DOI: 10.26418/positron.v15i1.92902

Influence of Alkaline and Acidic Co-precipitation Media on Fe_3O_4/TiO_2 Photocatalyst Performance for the Photodegradation of Cypermethrin

Sri Nengsih[a]*, Nawwar Syauqi Yansa[b], Sainur Fatikhin[b], Melsa Oktaviana[b], Nazhyra Shadrina[b], Siti Sarah[b], Nurul Adilah Lubis[b], Syarifah Raudhatul Jinan[b], Cut Nurul Mahya Irayana[b], Arief Rahman[b], Suardi Nur[b]

[a]Department of Physics Engineering, Science and Technology Faculty, Universitas Islam Negeri (UIN) Ar-Raniry Banda Aceh, Indonesia, 23111

[b]Department of Environmental Engineering, Science and Technology Faculty, Universitas Islam Negeri (UIN) Ar-Raniry Banda Aceh, Indonesia, 23111,

*Email: srinengsih@ar-raniry.ac.id

(Received 4 May 2025; Revised 12 May 2025; Accepted 21 May 2025; Published 31 May 2025)

Abstract

The persistence of pesticide residues such as cypermethrin in water bodies has raised environmental concerns, necessitating the development of effective photocatalytic materials for their degradation. This study examines the influence of solvent-assisted magnetite synthesis on the structural, magnetic, and photocatalytic properties of Fe_3O_4/TiO_2 composites for cypermethrin degradation under UV light with a focus on a comparative approach between alkaline and acidic synthesis routes, which has not been extensively reported. Fe_3O_4 was synthesized via co-precipitation using NaOH and HCl to assess the impact of solvent conditions. X-ray diffraction confirmed the spinel-phase structure in both samples, while SEM showed finer and more uniform particles in the NaOH-derived sample. VSM analysis revealed that Fe_3O_4–HCl exhibited higher saturation magnetization (Ms = 57.98 emu/g) but lower coercivity (Hc = 0.0206 T) than Fe_3O_4–NaOH (Ms = 41.26 emu/g; Hc = 0.0241 T), indicating synthesis-dependent magnetic properties. UV–Vis analysis identified a cypermethrin absorption peak at 220 nm, which was used to monitor degradation. The Fe_3O_4–NaOH:TiO_2 composite showed superior photocatalytic activity (31.98% degradation in 90 minutes) compared to Fe_3O_4–HCl:TiO_2 (22.86%). Kinetic modeling using the pseudo-first-order equation yielded a higher rate constant for Fe_3O_4–NaOH:TiO_2 ($k = 0.00172\ min^{-1}$; $R^2 = 0.769$), while Fe_3O_4–HCl:TiO_2 showed slower kinetics but better linearity ($k = 0.00030\ min^{-1}$; $R^2 = 0.9999$). These results suggest that alkaline synthesis enhances particle morphology and charge transfer efficiency, improving photocatalytic performance. Therefore, Fe_3O_4–NaOH:TiO_2 represents a promising candidate for cypermethrin remediation in wastewater treatment.

Keywords: Co-precipitation method, Cypermethrin degradation, Fe_3O_4–TiO_2 composite, Photocatalysis.

1. Introduction

The widespread use of synthetic pesticides in agriculture has played a crucial role in improving crop yields [1]. One such compound, cypermethrin, a Type II pyrethroid insecticide, is widely utilized due to its high efficacy, low volatility, and moderate environmental persistence [2]. However, cypermethrin exhibits poor water solubility and tends to accumulate in sediments and aquatic organisms, posing significant risks of neurotoxicity and broader ecotoxicological impacts[3].

To address water contamination by such persistent organic pollutants, heterogeneous photocatalysis has emerged as a promising green technology [4,5]. Among various photocatalytic materials, titanium dioxide (TiO_2) in its anatase phase has been extensively studied for its strong oxidative capability and excellent chemical stability [6–8]. Upon UV irradiation, TiO_2 generates electron-hole pairs [9,10], which initiate the formation of reactive oxygen species (ROS) capable of degrading organic contaminants into less harmful products. However, TiO_2 suffers from limitations such as poor visible light absorption and a high recombination rate of charge carriers, which restrict its photocatalytic efficiency [11,12].

To enhance the performance of TiO_2, researchers have developed composite systems by incorporating magnetic materials such as magnetite (Fe_3O_4) [13–16]. The resulting Fe_3O_4/TiO_2 composites offer improved charge separation and allow magnetic recovery, facilitating photocatalyst reuse and operational sustainability. Fe_3O_4 acts as an electron trap, suppressing charge recombination, while its magnetic properties enable straightforward post-reaction separation [12,17–19].

A commonly adopted method for synthesizing Fe_3O_4 is the co-precipitation technique [15,20,21], favored for its simplicity, low cost, and scalability. However, the structural and magnetic properties of Fe_3O_4—such as particle size, crystallinity, and saturation magnetization—are highly sensitive to synthesis conditions, particularly the chemical nature of the solvent or precipitating agent. While previous studies have examined the effects of precursor concentration and pH on magnetite formation, comparative investigations into the influence of acidic (e.g., HCl) versus alkaline (e.g., NaOH) solvents remain limited, especially with respect to their downstream impact on photocatalytic performance [22–24].

Furthermore, although Fe_3O_4/TiO_2 composites have been extensively evaluated for the degradation of dyes and pharmaceutical residues [25–28], studies specifically targeting the photodegradation of cypermethrin are scarce. Similarly, the correlation between Fe_3O_4 properties which are modified through different synthesis routes, and the resulting photocatalytic activity of the composites has not been comprehensively explored.

In light of these gaps, the present study aims to investigate the effect of solvent type (37% HCl vs. 3 M NaOH) on the synthesis of Fe_3O_4 via the co-precipitation method and its influence on the structural, morphological, and magnetic properties of Fe_3O_4/TiO_2 composites. Previous studies have shown that the choice of acidic or alkaline solvents in magnetite synthesis can significantly influence crystal growth, particle uniformity, and surface characteristics, which in turn affect the material's functionality [29,30]. The synthesized materials are subsequently applied for the photocatalytic degradation of cypermethrin under UV-A irradiation. This research seeks to contribute new insights into the design of efficient and magnetically recoverable photocatalysts for environmental remediation, particularly in the treatment of pesticide-contaminated wastewater.

2. Methodology

2.1 Materials

Magnetite (Fe_3O_4) was synthesized from natural iron sand sourced from Anoi Itam Beach, Sabang, Indonesia [15,31,32]. Anatase-phase titanium dioxide (TiO_2) was procured from a local supplier and used without further purification. All reagents, including 37% hydrochloric acid (HCl), 3 M sodium hydroxide (NaOH), ammonium hydroxide (NH_4OH), and ethanol, were of analytical grade and obtained from Merck. The insecticidal pesticide used in this study was a commercial cypermethrin formulation (250 EC). Ultrapure water (Type 1, Merck Millipore) was used for all solution preparations and dilutions. Experimental apparatus included standard laboratory glassware, filter paper, a LabTech shaking water bath, oven, mortar and pestle, sieves, a magnetic stirrer, a Fritsch P6 planetary ball mill, and UV-A lamps.

2.2 Synthesis of Magnetite and Fe_3O_4/TiO_2 Composite

Magnetite (Fe_3O_4) was synthesized from natural iron sand via the co-precipitation method [33,34]. Initially, iron sand collected from Anoi Itam Beach, Sabang, Indonesia, was subjected to magnetic separation using a bar magnet to isolate magnetically responsive particles. The collected material was sieved to remove coarse impurities, washed thoroughly with distilled water, and dried in an oven. The dried sand was then ground using a planetary ball mill (Fritsch P6) at 350 rpm for 5 hours to achieve finer particle sizes.

For the co-precipitation synthesis, 20 g of the milled iron sand was dissolved under two different solvent conditions to evaluate the influence of pH. In the acidic condition, the iron sand was dissolved in 50 mL of 37% hydrochloric acid (HCl) with an estimated pH of ~2. In the alkaline condition, it was dissolved in 50 mL of 3 M sodium hydroxide (NaOH) with an estimated pH of ~13. Each mixture was stirred at 800 rpm for 30 minutes while maintaining the temperature at 80°C. After filtration to remove insoluble residues, the filtrate was titrated dropwise with 6.5 M ammonium hydroxide (NH_4OH) solution until the pH reached approximately 7. This adjustment induced the co-precipitation of Fe^{2+} and Fe^{3+} ions to form magnetite nanoparticles [35,36]. The resulting black precipitate was filtered, washed repeatedly with distilled water to remove residual ions, and dried at 100°C for 1 hour.

The Fe_3O_4/TiO_2 photocatalyst composite was prepared by mixing the synthesized Fe_3O_4 with commercial anatase TiO_2 in a 1:1 weight ratio. The mixture was dispersed in 33% ethanol as a solvent and stirred in a shaking water bath at 130 rpm for

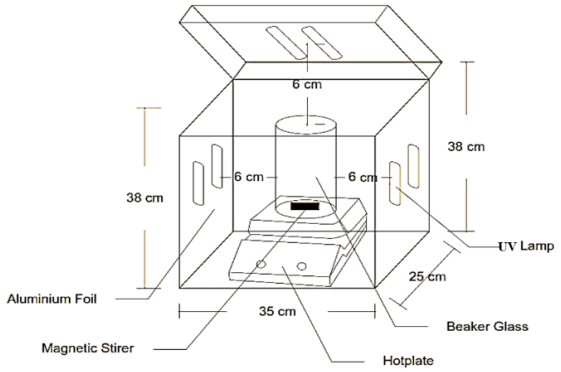

Figure 1. Design of Reactor Photodegradation

30 minutes to achieve uniform dispersion. The suspension was then filtered and oven-dried at 100°C for 1 hour. Finally, the dried composite powder was calcined in a muffle furnace at 500°C for 2 hours to improve structural stability and phase integration.

2.3 Photodegradation Procedure

A 10-ppm solution of cypermethrin was prepared as the model pollutant. The photocatalytic degradation test was conducted by adding 1.5 g of Fe_3O_4/TiO_2 photocatalyst into 2 L of the pesticide solution. The mixture was stirred in the dark for 30 minutes to reach adsorption-desorption equilibrium [15,25,37,38]. The suspension was then irradiated with UV-A light in a custom-designed reactor consisting of six 10-watt UV-A lamps arranged on the left, right, and top sides of the chamber for uniform light distribution. The reactor was equipped with reflective inner walls, a magnetic stirrer, and a reaction vessel to ensure continuous mixing and light utilization, is shown at Figure 1.

Following irradiation, 20 mL of the reaction mixture was sampled and centrifuged at 4000 rpm for 5 minutes. The supernatant was collected and analysed by UV-Vis spectrophotometry to determine the degradation efficiency based on absorbance changes. The magnetic property of Fe_3O_4 facilitated easy catalyst recovery and reuse [39], contributing to the sustainability of the process.

2.4 Characterization and Data Analysis

The crystalline structure of the synthesized photocatalyst was examined by X-ray diffraction (XRD) using a Shimadzu MAXima diffractometer (Cu Kα radiation, 40 kV, 30 mA). Average crystallite size was determined using the Scherrer equation [20,38], represented by the eq. (1)

$$D = \frac{K\,\lambda}{\beta \cos\theta} \qquad (1)$$

where D is the crystallite size (nm), K is the shape factor (0.9), λ is the X-ray wavelength (0.15406 nm), β is the FWHM of the diffraction peak in radians, and θ is the Bragg angle. The analysis was used to evaluate the influence of synthesis conditions on crystal growth and phase composition. Morphology was observed using a scanning electron microscope (SEM, Thermo Scientific Prisma E, Version 16.0) operating at 10 kV and 0.25 nA. Microstructural features such as particle size, agglomeration, and TiO_2 coating uniformity were analyzed. Magnetic properties were characterized using a vibrating sample magnetometer (VSM, OXFORD 1.2H). Magnetic hysteresis loops were measured using VSM to determine saturation magnetization (Ms), coercivity (Hc), and remanent magnetization (Mr) [25,40]. These values were analyzed to assess the efficiency of magnetic recovery and the effect of TiO_2 coating on magnetic properties. Photocatalytic performance in degrading cypermethrin was evaluated using a UV-Vis spectrophotometer (Perkin Elmer LAMBDA 365). The photocatalytic degradation of cypermethrin was quantified using degradation (%) [7].

$$Degradation = \frac{Co - Ct}{Co}\ x\ 100\ \% \qquad (2)$$

where C_0 and C_t are pollutant concentrations at time 0 and t, respectively. To further understand the reaction kinetics, the photocatalytic degradation was analyzed assuming a pseudo-first-order reaction mode [17]

$$\ln\frac{C_0}{C_t} = kt \qquad (3)$$

3. Results and Discussion

The crystallographic structure of magnetite (Fe_3O_4) synthesized using two different chemical precipitation pathways—NaOH-based and HCl-based—was examined using X-ray diffraction (XRD), and the corresponding patterns are shown in Figure 2.

Both samples exhibit characteristic diffraction peaks corresponding to the cubic inverse spinel structure of Fe_3O_4, indexed at (220), (311), (400), (422), (511), and (440) planes (JCPDS No. 19-0629) [25,41], indicating successful formation of

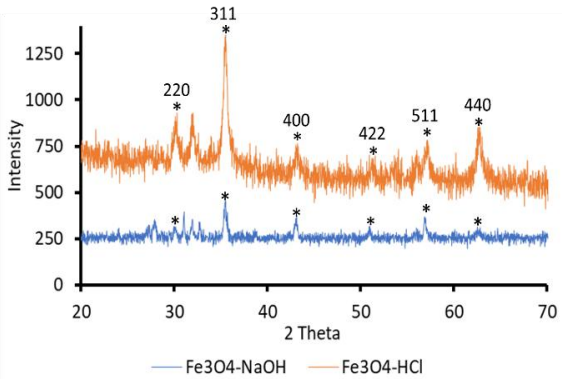

Figure 2. X-ray diffraction (XRD) patterns of Fe_3O_4 synthesized using NaOH-based and HCl-based solvents.

magnetite. The Fe_3O_4 synthesized using HCl as the solvent (orange pattern) exhibits significantly higher peak intensities compared to the NaOH-based synthesis (blue pattern), particularly at the most intense peak around 2θ = 35.5°, corresponding to the (311) plane. The sharper and more intense peaks suggest a higher degree of crystallinity in the HCl-derived Fe_3O_4 sample. In contrast, the NaOH-derived sample shows broader peaks with lower intensity, indicating smaller crystallite sizes and possibly the presence of amorphous or less-ordered domains.

Based on The Scherrer equation was employed using the (311) peak, the calculated crystallite sizes are: Fe_3O_4-NaOH: 12.3 nm and Fe_3O_4-HCl: 21.5 nm. These findings support the visual interpretation of the XRD patterns, confirming that the acidic synthesis route leads to larger and more crystalline Fe_3O_4 particles. This can be attributed to the gradual hydrolysis and controlled nucleation environment provided by the HCl medium, which allows for steady crystal growth. On the other hand, the high pH in NaOH solution accelerates the precipitation process, producing smaller particles with a higher degree of agglomeration and structural disorder. The differences in crystallite size and crystallinity are expected to influence the subsequent magnetic and photocatalytic performance of the Fe_3O_4/TiO_2 composites, as both properties are structure-sensitive [42].

Figure 3 illustrates the SEM images of Fe_3O_4 particles synthesized using NaOH and HCl as solvents. The morphological features observed are consistent with the crystallite sizes determined via XRD, where Fe_3O_4–NaOH exhibits a smaller crystallite size (12.3 nm) compared to Fe_3O_4–HCl (21.5 nm). The NaOH-based Fe_3O_4 sample displays a more porous and loosely aggregated morphology, characterized by finer particles with relatively rough and fragmented surfaces. This microstructure reflects the smaller crystallite size, which is commonly associated with a slower growth rate and higher nucleation density under basic synthesis conditions. The increased surface roughness and porosity may contribute to a larger surface area, which is beneficial for applications such as photocatalysis or adsorption.

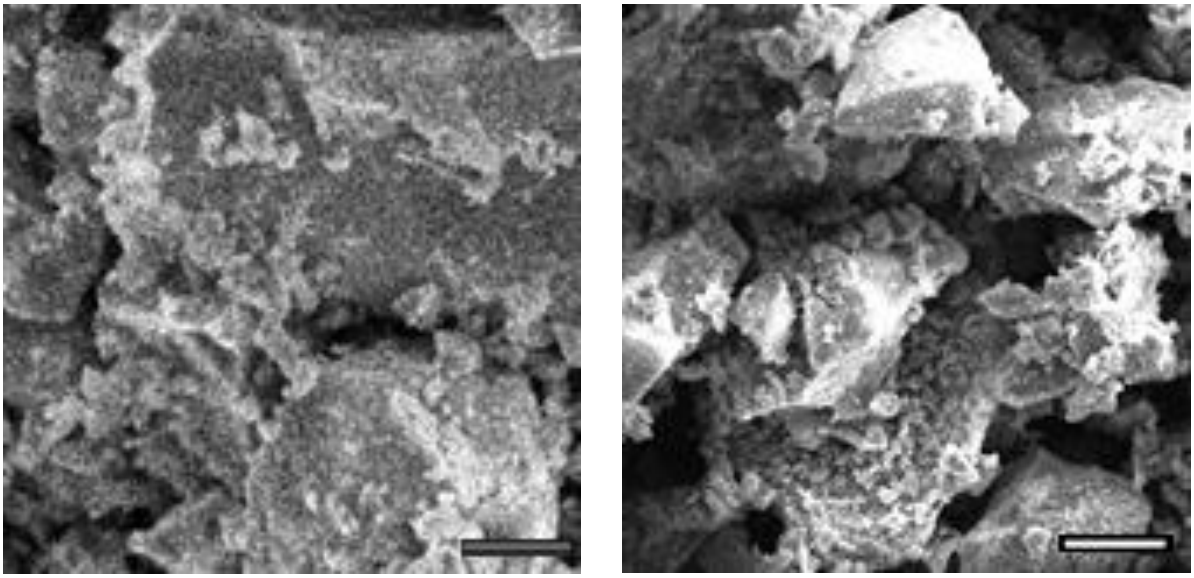

(a) (b)

Figure 3. The SEM images of Fe_3O_4 with (a) NaOH solvent, and (b) HCl solvent.

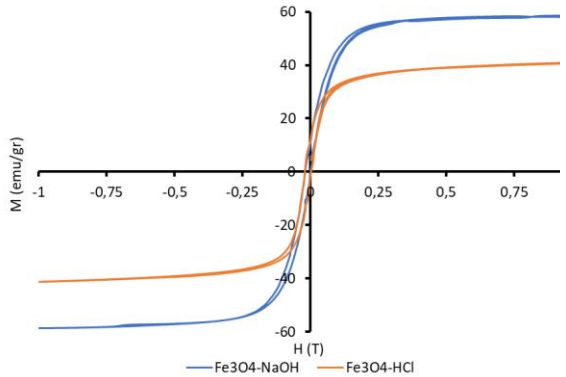

Figure 4. the hysteresis loops of Fe_3O_4 with difference solvent.

In contrast, the HCl-based Fe_3O_4 shows larger and more compact grain formations with smoother surfaces and clearer grain boundaries. The more consolidated and agglomerated texture suggests the dominance of crystal growth over nucleation in acidic conditions, resulting in a larger crystallite size. Such compact structures may lead to reduced surface accessibility and lower specific surface area, which can affect catalytic performance.

The SEM observations support the XRD-derived crystallite sizes, with NaOH promoting the formation of smaller, more reactive particles and HCl leading to larger, more crystalline aggregates.

The magnetic behavior of Fe_3O_4 nanoparticles synthesized using NaOH and HCl as precipitating agents was evaluated using Vibrating Sample Magnetometry (VSM). The resulting hysteresis loops are shown in Figure 4, and the key magnetic parameters, including saturation magnetization (Ms), remanent magnetization (Mr), and coercivity (Hc), are summarized in Table 1.

Table 1. Magnetic data of Fe_3O_4 synthesized using NaOH and HCl as precipitating agents

Sample	Ms (emu/gr)	Mr (emu/gr)	Hc (T)
Fe_3O_4-NaOH	41,255	13,312	0,0241
Fe_3O_4-HCl	57,975	12,055	0,0206

The Fe_3O_4-HCl sample exhibited a notably higher saturation magnetization (Ms) of 57.975 emu/g compared to 41.255 emu/g for the Fe_3O_4-NaOH sample. This higher Ms value indicates a greater alignment of magnetic domains and suggests that the HCl-mediated synthesis route produced particles with enhanced magnetic ordering. This result is consistent with the crystallite size data derived from X-ray diffraction (XRD), where Fe_3O_4-HCl exhibited a larger crystallite size (21.5 nm) than Fe_3O_4-NaOH (12.3 nm). Larger crystallites are generally associated with reduced surface spin disorder, contributing to increased net magnetic moments.

Interestingly, despite its lower saturation magnetization, the Fe_3O_4-NaOH sample showed a slightly higher remanent magnetization (Mr) of 13.312 emu/g compared to 12.055 emu/g for the Fe_3O_4-HCl sample. This observation suggests that the NaOH-based particles retain more magnetization after removing the external magnetic field. Such behavior may result from differences in particle morphology, surface area, or interparticle magnetic interactions, which are more pronounced in smaller particles with higher surface-to-volume ratios.

The coercivity (Hc) values for both samples were relatively low, with Fe_3O_4-NaOH at 0.0241 T and Fe_3O_4-HCl at 0.0206 T. These low Hc values indicate the superparamagnetic behavior [43–45], characterized by minimal magnetic hysteresis and the absence of magnetic remanence in the absence of an external field. Moreover, the slightly higher coercivity in the Fe_3O_4-NaOH sample may be attributed to its smaller crystallite size and increased magnetic anisotropy. Smaller particles are more susceptible to surface effects and magnetic frustration, which can hinder domain wall motion and require a higher field for magnetization reversal.

Overall, the Fe_3O_4-HCl nanoparticles demonstrated superior saturation magnetization, making them more suitable for applications requiring strong magnetic responsiveness. In contrast, the Fe_3O_4-NaOH nanoparticles, with higher remanence and coercivity, may be advantageous in applications with essential magnetic retention and stability. These findings highlight the importance of synthesis conditions in tailoring the magnetic properties of Fe_3O_4 nanoparticles for specific functional applications.

Following the characterization of the synthesized Fe_3O_4 nanoparticles, the photocatalytic activity of the Fe_3O_4–TiO_2 composite was evaluated through the degradation of cypermethrin under UV irradiation. Cypermethrin, a widely used pyrethroid pesticide, was selected as the target pollutant due to its persistence in aquatic environments and potential ecological hazards.

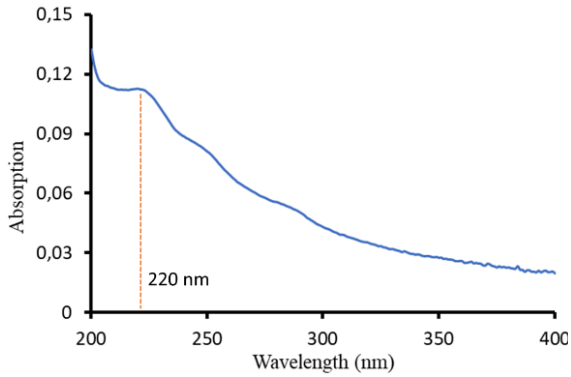

Figure 5. the UV–Vis's absorption spectrum of cypermethrin.

To initiate this analysis, cypermethrin's UV–Vis absorption spectrum was recorded to determine its characteristic absorption peak, which serves as the reference point for monitoring its concentration over time during the photodegradation process.

Figure 5 displays cypermethrin's UV–Vis absorption spectrum in aqueous solution, recorded in the wavelength range of 200–400 nm. Cypermethrin exhibits a prominent absorption peak at approximately 220 nm [46], corresponding to the π–π* electronic transition associated with its aromatic rings and conjugated structures. This characteristic peak serves as a reference wavelength for monitoring the degradation of cypermethrin under UV irradiation. The gradual decrease in absorbance at this wavelength over time indicates the breakdown of the molecular structure of cypermethrin, thus reflecting the progress of the photocatalytic degradation process.

Figure 6 presents the calibration curve of cypermethrin, constructed by plotting the absorbance values measured at 220 nm against a series of known concentrations ranging from 0 to 20 ppm. The resulting linear regression equation is given as: y=0.1187x−0.0628 with a high correlation coefficient of R^2 = 0.9802, indicating excellent linearity and suggesting that the absorbance response is directly proportional to cypermethrin concentration within the examined range. The slope of the curve (0.1187) represents the sensitivity of the UV–Vis spectrophotometric method toward cypermethrin, while the small y-intercept (−0.0628) implies minimal systematic error at low concentrations.

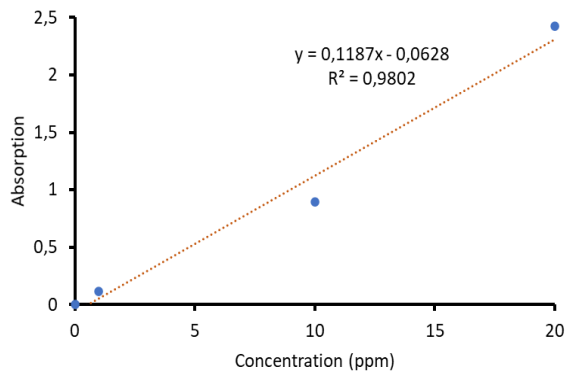

Figure 6. Calibration Curve of cypermethrin.

The strong linear relationship validates the use of this calibration model for quantitative analysis of cypermethrin during the photocatalytic degradation process. The corresponding concentrations of residual cypermethrin in solution can be accurately calculated by substituting the absorbance values from time-dependent degradation experiments into the regression equation. Furthermore, the closeness of the R^2 value to unity confirms the reliability and reproducibility of the spectrophotometric measurements. This calibration curve is a crucial reference for determining cypermethrin's degradation efficiency and kinetics under various photocatalytic treatment conditions.

The photodegradation efficiency of cypermethrin using magnetite–TiO_2 composites was investigated under UV irradiation. Two different synthesis routes for magnetite (Fe_3O_4) were compared: one using NaOH and the other using HCl as the solvent. The degradation percentages were plotted over a reaction time of 0 to 90 minutes, as presented in Figure 7.

The Fe_3O_4–NaOH:TiO_2 photocatalyst demonstrated significantly higher degradation

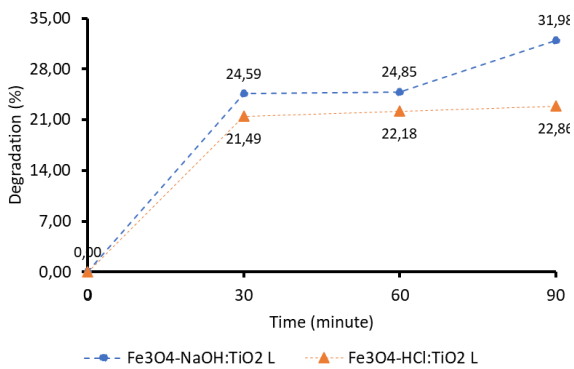

Figure 7. Percentage degradation pesticide cypermethrin using photocatalyst Fe_3O_4–NaOH:TiO_2 and Fe_3O_4–HCl:TiO_2 composite.

efficiency compared to the Fe_3O_4–HCl:TiO_2 counterpart. After 30 minutes of irradiation, the Fe_3O_4–NaOH:TiO_2 achieved a degradation of 24.59%, while Fe_3O_4–HCl:TiO_2 reached 21.49%. Over time, the performance gap widened: at 60 minutes, the NaOH-synthesized composite maintained a stable efficiency of 24.85%, whereas the HCl-based catalyst slightly decreased to 22.18%. After 90 minutes, the degradation efficiency of Fe_3O_4–NaOH:TiO_2 further increased to 31.98%, while Fe_3O_4–HCl:TiO_2 plateaued at 22.86%.

These results suggest that the synthesis medium plays a crucial role in determining the photocatalytic activity of the resulting material. The higher activity of the NaOH-based catalyst may be attributed to better crystallinity, higher surface area, or improved electron-hole separation efficiency due to more favorable physicochemical properties imparted during synthesis. Alkaline conditions during synthesis may promote the formation of smaller and more uniformly distributed Fe_3O_4 nanoparticles, enhancing the interaction with TiO_2 and improving charge transfer dynamics. Moreover, the slower degradation rate of the Fe_3O_4–HCl:TiO_2 composite suggests possible agglomeration or formation of larger Fe_3O_4 particles under acidic synthesis conditions, which could reduce the active surface area and hinder photocatalytic performance. Overall, the Fe_3O_4–NaOH:TiO_2 photocatalyst exhibits superior photocatalytic performance in degrading cypermethrin pesticide.

To further investigate the degradation mechanism of cypermethrin, the experimental data were evaluated using a pseudo-first-order kinetic model, in shown at Figure 8. The degradation data for both Fe_3O_4–NaOH:TiO_2 and Fe_3O_4–HCl:TiO_2 photocatalysts were plotted as Ln (Co/Ct) versus time, and the rate constants were determined from the slope of the linear regression lines. The results revealed that Fe_3O_4–NaOH:TiO_2 had a higher rate constant, k = 0.00172 min^{-1}, compared to Fe_3O_4–HCl:TiO_2, which showed a lower value of k = 0.00030 min^{-1}. This suggests that the NaOH-synthesized photocatalyst facilitated a faster degradation of cypermethrin under the same conditions. However, the coefficient of determination (R^2) for the NaOH-based catalyst was 0.769, indeed catalyst demonstrated an exceptional linear fit with R^2 = 0.9999, implying a more consistent and predictable kinetic behavior, albeit with a slower degradation rate.

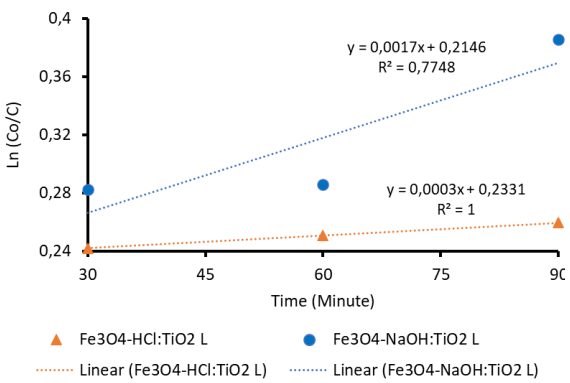

Figure 8. Kinetic Modeling of Photodegradation pesticide cypermethrin using photocatalyst Fe_3O_4–NaOH: TiO_2 and Fe_3O_4–HCl: TiO_2 composite.

These findings suggest that while Fe_3O_4–NaOH:TiO_2 may offer a more aggressive catalytic activity initially, its behavior over time may deviate from ideal first-order kinetics, possibly due to surface saturation, intermediate product accumulation, or catalyst surface properties. On the other hand, Fe_3O_4–HCl:TiO_2 exhibits more uniform kinetic behavior, which may be advantageous for applications requiring steady-state degradation. Both photocatalysts are capable of degrading cypermethrin under UV light, with Fe_3O_4–NaOH:TiO_2 demonstrating higher activity but slightly less conformity to the kinetic model and Fe_3O_4–HCl:TiO_2 offering a slower but more linear degradation profile.

The collective results from XRD, SEM, VSM, and photocatalytic performance tests demonstrate that the synthesis environment substantially affects the physicochemical and functional attributes of Fe_3O_4–TiO_2 composites. Under alkaline conditions (NaOH), the formation of smaller crystallites and more uniform morphologies was observed, favoring higher surface area and enhanced interfacial contact between Fe_3O_4 and TiO_2 [47]. These morphological advantages support improved electron–hole separation and reduced recombination rates [16,48], as reflected in the superior degradation efficiency (31.98%) and higher reaction rate constant (k = 0.00172 min^{-1}) for cypermethrin.

Although Fe_3O_4–HCl exhibited a higher saturation magnetization (Ms = 57.98 emu/g), this likely stems from its larger crystalline domains and reduced surface spin disorder, which do not necessarily translate into better photocatalytic performance. The lower activity of the acidic-derived composite may be attributed to particle agglomeration, reduced surface accessibility, and weaker interfacial interaction with TiO_2. The higher coercivity and remanence in the NaOH-derived composite further suggest enhanced surface anisotropy and electron trapping capacity, aligning with prior findings on the role of magnetic properties in promoting photocatalytic efficiency [49–51].

The divergence in kinetic profiles, characterized by the faster yet less linear degradation behaviour observed with the NaOH-based composite compared to the slower but highly linear kinetics of the HCl-based system, indicates a trade-off between catalytic aggressiveness and modelling predictability. These trends correspond with earlier reports emphasizing how synthesis parameters, including pH and precipitation rate, affect not only the crystalline and magnetic features but also the photocatalytic dynamics of Fe_3O_4-based systems.

Overall, the alkaline co-precipitation route yields composites with more favorable characteristics for photocatalytic degradation, underlining the importance of synthesis parameters in optimizing multifunctional nanocomposites for environmental applications.

4. Conclusion

Fe_3O_4–TiO_2 photocatalysts synthesized via NaOH and HCl precipitation routes exhibit notable differences in structure, morphology, magnetism, and photocatalytic performance. XRD analysis confirmed the formation of magnetite with high crystallinity, while SEM observations showed that Fe_3O_4–NaOH had smaller, more uniformly distributed particles, likely contributing to better interfacial contact with TiO_2. Magnetic characterization revealed that Fe_3O_4–HCl possessed higher magnetic saturation, whereas Fe_3O_4–NaOH showed slightly higher coercivity, indicating different magnetic domain behaviors. Photocatalytic tests against cypermethrin demonstrated that Fe_3O_4–NaOH:TiO_2 outperformed the HCl-based composite, achieving 31.98% degradation within 90 minutes under UV irradiation. Despite its lower magnetic response, the NaOH-derived catalyst showed enhanced photodegradation kinetics, attributable to superior particle dispersion and charge transfer efficiency. Kinetic modeling supported these findings, with Fe_3O_4–NaOH:TiO_2 having a faster reaction rate but lower model conformity, while Fe_3O_4–HCl:TiO_2 exhibited slower yet more predictable degradation behavior. Overall, the synthesis route critically influences the physicochemical properties and photocatalytic capabilities of Fe_3O_4–TiO_2 composites, with alkaline-synthesized materials showing greater potential for environmental remediation applications involving persistent organic pollutants like cypermethrin.

5. Acknowledgment

The authors gratefully acknowledge the Laboratory of Multifunctional Materials at UIN Ar-Raniry Banda Aceh for granting access to the UV-Vis spectrophotometer. Appreciation is also extended to the Chemistry Laboratory for their support throughout the synthesis and photocatalytic testing stages. The authors further thank the Physics Laboratory at Universitas Syiah Kuala (USK) Banda Aceh for enabling the XRD analysis. Special thanks are due to the technical staff, Syarifah Fathmiyah, M.Sc., Nizar Mauliza, S.Si., and Rizki Kurniawan, M.Si. as well as the student collaborators for their crucial contributions in sample preparation and reactor assembly.

References

[1] Zeshan, M. , Bhatti, I. A. , Mohsin, M. , Iqbal, M. , Amjed, N. , Nisar, J. , AlMasoud, N. , and Alomar, T. S. , Remediation of pesticides using TiO2 based photocatalytic strategies: A review, Chemosphere, 300(March), pp.134525, 2022.

[2] Kansal, I. , Kapoor, A. , Solanki, S. , and Singh, R. , Cypermethrin toxicity in the environment: analytical insight into detection methods and microbial degradation pathways, Journal of Applied Microbiology, 134(6), pp.1–12, 2023.

[3] Environment Agency , Cypermethrin: Sources, pathways and environmental data, Bristol, (October), 2019.

[4] Bisaria, K. , Sinha, S. , Singh, R. , and Iqbal, H. M. N. , Recent advances in structural modifications of photocatalysts for organic pollutants degradation – A comprehensive review, Chemosphere, 284(June), pp.131263,

2021.
[5] Kalidhasan, S. and Lee, H. Y. , Preparation of TiO2-deposited silica-based catalysts for photocatalytic decomposition of chloro-pesticide to environmentally less toxic species, Chemosphere, 290(December 2021), pp.133300, 2022.
[6] Celia, C., Marsooli, M. A., Rahimi-nasrabadi, M., and Fasihi-ramandi, M. , Preparation of Fe_3O_4/ SiO_2/TiO_2/$CeVO_4$ Nanocomposites: Investigation of Photocatalytic Effects on Organic Pollutants , Bacterial Environments , and New Potential Therapeutic Candidate Against Cancer Cells11(March), pp.1–15, 2020.
[7] Hernandez-Del, C. P. C. , Oliva, J. , and Rodriguez-Gonzalez, V. , An eco-friendly and sustainable support of agave-fibers functionalized with graphene / TiO2 : SnO2 for the photocatalytic degradation of the 2 , 4-D herbicide from the drinking water, Journal of Environmental Management, 317 (11551(January), 2022.
[8] Djellabi, R. , Yang, B. , Adeel Sharif, H. M. , Zhang, J. , Ali, J. , and Zhao, X. , Sustainable and easy recoverable magnetic TiO2-Lignocellulosic Biomass@Fe3O4 for solar photocatalytic water remediation, Journal of Cleaner Production, 233pp.841–847, 2019.
[9] Iman Amir, M. N. , Julkapli, N. M. , Bagheri, S. , and Yousefi, A. T. , TiO2 hybrid photocatalytic systems: Impact of adsorption and photocatalytic performance, Reviews in Inorganic Chemistry, 35(3), pp.151–178, 2015.
[10] Balassa, L. , Ágoston, Á. , Kása, Z. , Hornok, V. , and Janovák, L. , Surface sulfate modified TiO2 visible light active photocatalyst for complex wastewater purification: Preparation, characterization and photocatalytic activity, Journal of Molecular Structure, 1260pp.132860, 2022.
[11] Ismael, M. , Latest progress on the key operating parameters affecting the photocatalytic activity of TiO2-based photocatalysts for hydrogen fuel production: A comprehensive review, Fuel, 303(April), pp.121207, 2021.
[12] Harifi, T. and Montazer, M. , A novel magnetic reusable nanocomposite with enhanced photocatalytic activities for dye degradation, Separation and Purification Technology, 134pp.210–219, 2014.
[13] Khashan, S. , Dagher, S. , Tit, N. , Alazzam, A. , and Obaidat, I. , Novel method for synthesis of Fe3O4@TiO2 core/shell nanoparticles, Surface and Coatings Technology, 322pp.92–98, 2017.
[14] Beduk, F. , Superparamagnetic nanomaterial Fe3O4–TiO2 for the removal of As(V) and As(III) from aqueous solutions, Environmental Technology, 37(14), pp.1790–1801, 2016.
[15] Nengsih, S. , Nur Abdulmadjid, S. , Mursal, M. , and Jalil, Z. , Photocatalytic performance of Fe3O4-TiO2 in the degradation of methylene blue dye: Optimizing the usability of natural iron sand, Materials Science for Energy Technologies, 7(May), pp.374–380, 2024.
[16] Kubiak, A. , Comparative study of TiO2–Fe3O4 photocatalysts synthesized by conventional and microwave methods for metronidazole removal, Scientific Reports, 13(1), pp.1–13, 2023.
[17] MirzaHedayat, B. , Noorisepehr, M. , Dehghanifard, E. , Esrafili, A. , and Norozi, R. , Evaluation of photocatalytic degradation of 2,4-Dinitrophenol from synthetic wastewater using Fe3O4@SiO2@TiO2/rGO magnetic nanoparticles, Journal of Molecular Liquids, 264pp.571–578, 2018.
[18] Zhao, X. , Wang, R. , Lu, Z. , Wang, W. , and Yan, Y. , Dual sensitization effect and conductive structure of Fe3O4@mTiO2/C photocatalyst towards superior photodegradation activity for bisphenol A under visible light, Journal of Photochemistry and Photobiology A: Chemistry, 382pp.111902, 2019.
[19] Fawzi Suleiman Khasawneh, O. and Palaniandy, P. , Removal of organic pollutants from water by Fe2O3/TiO2 based photocatalytic degradation: A review, Environmental Technology and Innovation, 21pp.101230, 2021.
[20] Jesus, A. C. B. , Jesus, J. R. , Lima, R. J. S. , Moura, K. O. , Almeida, J. M. A. , Duque, J. G. S. , and Meneses, C. T. , Synthesis and magnetic interaction on concentrated Fe3O4 nanoparticles obtained by the co-precipitation and hydrothermal chemical methods, Ceramics International, 46(8), pp.11149–11153, 2020.
[21] Radoń, A. , Drygała, A. , Hawełek, Ł. , and Łukowiec, D. , Structure and optical properties of Fe3O4 nanoparticles synthesized by co-precipitation method with different organic modifiers, Materials Characterization, 131pp.148–156, 2017.
[22] Rahmawati, R. , Permana, M. G. , Harison, B. , Nugraha , Yuliarto, B. , Suyatman , and Kurniadi, D. , Optimization of Frequency and Stirring Rate for Synthesis of Magnetite (Fe3O4) Nanoparticles by Using Coprecipitation- Ultrasonic Irradiation Methods, Procedia Engineering, 170pp.55–59,

2017.
[23] Nengsih, S. , Madjid, S. N. , Mursal , and Jalil, Z. , Synthesis and characterization of magnetite particles from Syiah Kuala iron sand prepared by co-precipitation method, Journal of Physics: Conference Series, 2582(012005), pp.1–7, 2023.
[24] Venkateswarlu, S. , Kumar, B. N. , Prathima, B. , SubbaRao, Y. , and Jyothi, N. V. V. , A novel green synthesis of Fe 3 O 4 magnetic nanorods using Punica Granatum rind extract and its application for removal of Pb(II) from aqueous environment, Arabian Journal of Chemistry, 12(4), pp.588–596, 2019.
[25] Zhang, Q. , Yu, L. , Xu, C. , Zhang, W. , Chen, M. , Xu, Q. , and Diao, G. , A novel method for facile preparation of recoverable Fe3O4@TiO2 core-shell nanospheres and their advanced photocatalytic application, Chemical Physics Letters, 761(August), 2020.
[26] Afzal, S. , Julkapli, N. M. , and Mun, L. K. , Visible light active TiO2/CS/Fe3O4 for nitrophenol degradation: Studying impact of TiO2, CS and Fe3O4 loading on the optical and photocatalytic performance of nanocomposite, Materials Science in Semiconductor Processing, 131(November 2020), pp.105891, 2021.
[27] Mufti, N. , Munfarriha, U. , Fuad, A. , and Diantoro, M. , Synthesis and photocatalytic properties of Fe3O4@TiO2 core-shell for degradation of Rhodamine B, AIP Conference Proceedings, 1712(February 2016), 2016.
[28] Govindhan, P. , Pragathiswaran, C. , and Chinnadurai, M. , A magnetic Fe3O4 decorated TiO2 nanoparticles application for photocatalytic degradation of methylene blue (MB) under direct sunlight irradiation, Journal of Materials Science: Materials in Electronics, 29(8), pp.6458–6469, 2018.
[29] Heryanto, H. and Tahir, D. , The correlations between structural and optical properties of magnetite nanoparticles synthesised from natural iron sand, Ceramics International, 47(12), pp.16820–16827, 2021.
[30] Rahmayanti, M. , Santosa, S. J. , Sutarno, S. , Hamidi, H. , and Binagara, L. , Synthesis, Characterization, and Application of Magnetite (Fe3O4) Particles as Gold Adsorbent from Simulation Waste, CHEMICA: Jurnal Teknik Kimia, 7(2), pp.151, 2021.
[31] Nengsih, S. , Karakteristik Nanopartikel Magnetite Besi Oksida Lampanah Aceh Besar Melalui Metode Kopresipitasi, Elkawnie, 5(1), pp.76, 2019.
[32] Nengsih, S. , Abdulmajid, S. N. , Mursal , and Jalil, Z. , Magnetization Study of Iron Sand from Sabang , Indonesia : The Potential of Magnetic Materials in the, Bulletin of Chemical Reaction Engineering & Catalysis (BCREC), 18(2), pp.344–352, 2023.
[33] Sunaryono , Taufiq, A. , Mashuri , Pratapa, S. , Zainuri, M. , Triwikantoro , and Darminto , Various magnetic properties of magnetite nanoparticles synthesized from iron-sands by coprecipitation method at room temperature, Materials Science Forum, 827(June), pp.229–234, 2015.
[34] Mufti, N. , Atma, T. , Fuad, A. , and Sutadji, E. , Synthesis And Characterization Of Black , Red And Yellow Nanoparticles Pigments From The Iron Sand, AIP Conference Proceeding, 165(2014), 2018.
[35] Liu, H. and Valentin, C. Di , Band Gap in Magnetite above Verwey Temperature Induced by Symmetry Breaking, The Journal of Physical Chemistry C, 121(46), pp.25736–25742, 2017.
[36] Priyadarshana, G. , Kottegoda, N. , Senaratne, A. , Alwis, A. De , and Karunaratne, V. , Synthesis of magnetite nanoparticles by top-down approach from a high purity ore, Journal of Nanomaterials, 20152015.
[37] Vinosel, V. M. , Anand, S. , Janifer, M. A. , Pauline, S. , Dhanavel, S. , Praveena, P. , and Stephen, A. , Preparation and performance of Fe3O4/TiO2 nanocomposite with enhanced photo-Fenton activity for photocatalysis by facile hydrothermal method, Applied Physics A: Materials Science and Processing, 125(5), pp.1–13, 2019.
[38] AbouSeada, N. , Ahmed, M. A. , and Elmahgary, M. G. , Synthesis and characterization of novel magnetic nanoparticles for photocatalytic degradation of indigo carmine dye, Materials Science for Energy Technologies, 5pp.116–124, 2022.
[39] Al-Salihi, S. , Bayati, M. , Jasim, A. M. , Fidalgo, M. M. , and Xing, Y. , Magnetic mesoporous TiO2/Fe3O4 nanocomposite adsorbent for removal of sulfamethazine from water, Environmental Advances, 9(August), pp.100283, 2022.
[40] Nkurikiyimfura, I. , Wang, Y. , Safari, B. , and Nshingabigwi, E. , Temperature-dependent magnetic properties of magnetite nanoparticles synthesized via coprecipitation method, Journal of Alloys and Compounds, 8462020.
[41] Dubey, M. , Kumar, R. , Srivastava, S. K. , and Joshi, M. , Visible light induced photodegradation of chlorinated organic pollutants using highly efficient magnetic Fe3O4/TiO2 nanocomposite, Optik,

243pp.167309, 2021.
[42] Wang, X. , Sø, L. , Su, R. , Wendt, S. , Hald, P. , Mamakhel, A. , Yang, C. , Huang, Y. , Iversen, B. , and Besenbacher, F. , The influence of crystallite size and crystallinity of anatase nanoparticles on the photo-degradation of phenol, Journal of Catalysis, 310pp.100–108, 2014.
[43] Jiang, Q. and Zhu, R. , Facile synthesis of highly efficient and cost-effective photo-Fenton catalyst by ball milling commercial TiO2 and natural magnetite, Journal of Alloys and Compounds, 862pp.158670, 2021.
[44] Iwasaki, T. , Mizutani, N. , Watano, S. , Yanagida, T. , and Kawai, T. , Size control of magnetite nanoparticles by organic solvent-free chemical coprecipitation at room temperature, Journal of Experimental Nanoscience, 5(3), pp.251–262, 2010.
[45] Baumgartner, J. , Bertinetti, L. , Widdrat, M. , Hirt, A. M. , and Faivre, D. , Formation of Magnetite Nanoparticles at Low Temperature: From Superparamagnetic to Stable Single Domain Particles, PLoS ONE, 8(3), pp.1–6, 2013.
[46] Shaheed, I. M. and Dhahir, S. A. , Extraction and determination of alpha-Cypermethrin in environmental samples from Kerbala city / Iraq and in its formulation using high performance liquid chromatography (HPLC)., IOP Conference Series: Materials Science and Engineering, 871(1), 2020.
[47] Kunarti, E. S. , Kartini, I. , Syoufian, A. , and Widyandari, K. M. , Syntehsis and Photoactivity of Fe3O4/TiO2-Co as a Magnetically Separable Visible Light Responsive Photocatalyst, Indonesian Journal of Chemistry, 18(3), pp.403–410, 2018.
[48] Gunlazuardi, J. , Fisli, A. , Ridwan , Krisnandi, Y. K. , and Robert, D. , Magnetically Separable Fe3O4/SiO2/TiO2 Photocatalyst Composites Prepared through Hetero Agglomeration for the Photocatalytic Degradation of Paraquat, Makara Journal of Science, 25(4), pp.236–246, 2021.
[49] Mansour, H. , Omri, K. , Bargougui, R. , and Ammar, S. , Novel α-Fe2O3/TiO2 nanocomposites with enhanced photocatalytic activity, Applied Physics A: Materials Science and Processing, 126(3), 2020.
[50] Mu, Q. , Sun, Y. , Guo, A. , Yu, X. , Xu, X. , Cai, A. , and Wang, X. , Biolated synthesis of Fe3O4-TiO2 composites derived from Chlorella pyrenoidosa with enhanced visible-light photocatalytic performance, Materials Research Express, 6(9), 2019.
[51] Hong, T. , Mao, J. , Tao, F. , and Lan, M. , Recyclable magnetic titania nanocomposite from ilmenite with enhanced photocatalytic activity, Molecules, 22(12), 2017.